frontiers | Frontiers in Marine Science

ORIGINAL RESEARCH
published: 22 June 2022
doi: 10.3389/fmars.2022.848756

Subsurface Water Property Structures Along 80°E Under the Positive Indian Ocean Dipole Mode in December 2019

Shinya Kouketsu[1]*, *Akihiko Murata*[1] and *Kanapathipillai Arulananthan*[2]

[1] Research Institute for Global Change, Japan Agency for Marine-Earth Science and Technology, Yokosuka, Japan, [2] National Institute of Oceanography Marine Sciences, National Aquatic Resources Research and Development Agency, Colombo, Sri Lanka

OPEN ACCESS

Edited by:
Gilles Reverdin, Centre National de la Recherche Scientifique (CNRS), France

Reviewed by:
SungHyun Nam, Seoul National University, South Korea
Ming Feng, Commonwealth Scientific and Industrial Research Organisation (CSIRO), Australia

***Correspondence:**
Shinya Kouketsu
skouketsu@jamstec.go.jp

Specialty section:
This article was submitted to Ocean Observation, a section of the journal Frontiers in Marine Science

Received: 05 January 2022
Accepted: 23 May 2022
Published: 22 June 2022

Citation:
Kouketsu S, Murata A and Arulananthan K (2022) Subsurface Water Property Structures Along 80°E Under the Positive Indian Ocean Dipole Mode in December 2019. Front. Mar. Sci. 9:848756. doi: 10.3389/fmars.2022.848756

High-accuracy ship-based observations were conducted at 80°E in the Indian Ocean. Salinity below the mixed layer in 2019 was observed to be lower than that in 1995. This decrease in salinity was mainly attributed to anomalous advection associated with one of the strongest positive Indian Ocean dipole (pIOD) events in 2019 through analysis of the gridded time series of the salinity distributions based on the Argo float array. Increases and decreases in nitrate and dissolved inorganic carbon (DIC) and dissolved oxygen (DO), respectively, were also detected on the isopycnal surfaces where decreases in salinity were observed, suggesting that the anomalous upwelling and westward advection associated with the pIOD in the eastern part of the equatorial region resulted in low-salinity, low-oxygen, and nutrient-rich waters in the central off-equatorial region of the Indian Ocean. However, downward isopycnal heaving, which was also associated with the pIOD, was too strong to have increased nitrate below the mixed layers, and thus might have suppressed biological activity. The heaving also affected the DIC and DO distributions, and the effect of interannual changes such as those associated with the Indian Ocean dipole is essential to estimating changes in anthropogenic carbon storage. This research represents a case study, based on only two occupations; therefore, an assessment utilizing more intensive observations and more realistic numerical simulations is necessary in the future.

Keywords: Positive Indian Ocean dipole, dissolved oxygen (DO), anthropogenic carbon dioxide, salinity changes, isopycnal changes

INTRODUCTION

Circulation in the Indian Ocean exhibits high variability owing to the equally high variability of forcings such as monsoons and the exchanges associated with the Indonesian Throughflow (ITF). In particular, salinity and temperature variabilities in the surface layers have been investigated in detail

using numerical model results as well as satellite and hydrographic observations. For example, changes in the freshwater input associated with river and precipitation are shown to contribute to important for seasonal variability of the mixed layer salinity in the Bay of Bengal, while horizontal advection changes also contribute to the changes in the mixed layer salinities north of the equator of the Indian Ocean (Rao and Sivakumar, 2003). In the southeastern equatorial region in the Indian Ocean (east of 100°E), seasonal changes in the mixed layer salinity are revealed by the balance among freshwater advection associated with the ITF (from the Pacific to the Indian Oceans through the Indonesian maritime continent), South Equatorial Current (along 12°S), and Leeuwin Current (along the west coast of the Australia), as well as with salty water entrainment at the bottom of the mixed layers and freshwater flux at sea surface. Meanwhile, the seasonal changes, especially in in the north region, resemble those ofsurface freshwater fluxes (Zhang et al., 2016). The interannual variability of salinity and sea surface temperature (SST) has also been reported. The Indian Ocean dipole (IOD) is one of the major climatological SST patterns driven by air-sea interactions in the Indian Ocean (Saji et al., 1999). During the positive IOD (pIOD), low-salinity water extends to the west around the equator due to the anomalous westward current (Thompson et al., 2006; Zhang et al., 2013). Furthermore, interannual salinity changes in the mixed layers are shown to be modified by changes in the precipitation around Indonesia associated with the El Nino-Southern Oscillation (ENSO; Hu and Sprintall, 2016).

It has been shown that variability in the Indian Ocean reflecting changes in the distribution of temperature and salinity, could result in complex variability of environmental changes that in turn reflect changes in the distribution of biogeochemical variables. For example, mooring and satellite observations at approximately 0° and, 80.5°E have shown high-frequency chlorophyll-a increases at sea surfaces associated with strong winds, intensified ocean current shear, and southward flow anomalies (Strutton et al., 2015). Satellite observations have captured increases in the chlorophyll-a concentration in the southeastern equatorial region (90°E–110°E, 10°S–0°) and decreases in the western equatorial region (50°E–70°E), which are caused by upwelling in the eastern region and depression of subsurface nutrient-rich water in the western region (Shi and Wang, 2021). The upwelling and depression have been associated with pIOD mode event. The anomalous upwelling of the nutrient-rich water in the southeastern equatorial regions could affect more broad changes in the water properties of subsurface layers. For example, detailed salinity changes associated with the IOD in the subsurface layers have been investigated in previous studies (e.g., Kido et al., 2019). Furthermore, interannual changes in salinity in the off-equatorial and subtropical regions in the layer of potential density of 24–25 kg m^{-3}, which are associated with Rossby wave propagation and advection of subducted waters, have been reported (e.g., Li and Wang, 2015; Nagura and Kouketsu, 2018) based on intensive observations using an Argo array. It has been found that local changes in the subsurface layers (below mixed layer depths) are not directly associated with surface flux changes (ex. precipitation and evaporations), while anomalous currents associated with Rossby wave propagations mainly caused salinity anomalies on isopycnal surfaces near the equatorial region around 11°–6°S, and the low and high salinity anomalies repeatedly (with periods of 2-3 yrs) propagated from west to east. In the subtropical regions around 12°S, salinity changes are associated with changes in water mass formation off the western coast of Australia, while high (low) salinity anomalies extended to the western part of the Indian Ocean from 2005 to 2007 (2012 to 2014). Furthermore, salinity changes are also influenced by the changes in the ITF (Hu et al., 2019). However, observations of various biogeochemical variables, especially observations below the sea surface, are insufficient to describe such variability and climatological events, whereas the subsurface salinity changes due to the changes in currents might be associated with spatially broad changes in the biochemical environment of subsurface layers.

In 2019, we observed the meridional section along 80°E (I08N World Ocean Circulation Experiment Hydrographic Programme line) under GO-SHIP (https://www.go-ship.org), an international ship observation network which provides the high-reliablility observations and high-accuracy measurements based on careful quality controls. Approximately 24 years have passed since a similar study was conducted in 1995. In this study, we describe changes in biogeochemical variables in subsurface layers based on these high-accuracy data. Particularly, changes in the distribution of biogeochemical materials associated with pIOD events has not been well studied due to there being less observations in the Indian Ocean. Since salinity distribution changes have been thoroughly investigated in previous studies (e.g., Hu et al., 2019; Kido et al., 2019), we compare the changes in salinity along the section and monthly anomalies based on the Argo float array and try to describe the relationship between changes in salinity and biogeochemical properties under the pIOD event along the observational section. The target pIOD event in 2019 was among the strongest of many (Doi et al., 2020a) and was found to have greatly influenced the early summer rainfall near Japan (Takaya et al., 2020) as well as the winter conditions in East Asia (Doi et al., 2020b). As IOD events mainly influence on upper water layers (ex. Kido et al., 2019, who focused on the layers above 150 dbar), we compared water property distributions mainly in the upper layers (above 500 dbar) in 1995 and 2019 to describe the detailed changes under the influence of the pIOD. We attempted to assess changes by comparing the possible influences of the events with the subsurface salinity variabilities revealed using the Argo float array.

DATA AND METHODS

GO-SHIP Type Observations

The I08N line (nominally along 80°E) was occupied in March and September 1995 during the World Ocean Circulation

Experiment. Following multiple cruises conducted during the 1990s (316N14_7 by R/V Knorr and 3175MB95_07 by R/V_Malcolm Baldrige; Swift and Becker, 2019a; Swift and Becker, 2019b), we conducted similar observations under GO-SHIP (**Figure 1**) in December 2019 (Uchida et al., 2021). The stations were meridionally set at intervals of approximately 0.5°. During the 1995 cruises, water sampling was conducted at every station, whereas in 2019, samplingwas at every other station. These cruises provide the most accurate measurements of various water properties from the surface to the bottom, utilizing conductivity-temperature-depth (CTD) sensors and water sampling following the same observation methods and careful quality controls of the procedures in the GO-SHIP manual (Hood et al., 2010). The temperature sensors were calibrated with a highaccuracy sensor (SEB35; Sea Bird Scientific USA) to remove small biases due to pressure sensitivity, viscous heating, and the temporal drift (Uchida et al., 2015), and the standard deviations of the differences from the reference value were less than 0.003 K, including in the region above 1950 dbar. Salinity sensors were corrected onboard with the bottle-sampled salinity measured by Autosal (Guildline Instruments Canada) with standard seawater, and the standard deviations from the bottle samples were < 0.005. Nutrients and dissolved inorganic carbon (DIC) were measured on board and corrected with the certified reference materials (produced by KANSO Co., Ltd. for nutrients and provided by Dr. A. G. Dickson at Scripps Institution of Oceanography), and the analytical precisions were less than 0.8% for nutrients and 2 μmol kg^{-1} for DIC, respectively. Measurements and quality controls of dissolved oxygen (DO) followed the GO-SHIP manual guidelines and the analytical uncertainties were less than 0.5 μmol kg^{-1}, while there was no reference for the measurements. The accuracy of measurements was similar to that in multiple assessments based on global observations in previous studies (Johnson et al., 2001; Lauvset et al., 2022). These cruises enabled the determination of water property structures from the south of Sri Lanka, across the equator, to the center of the subtropical gyre in the Indian Ocean (e.g., see **Figure S1 in the Supplement**). In 2019, as the southernmost station was located at 20.5°S, we focused on the changes from 20°S to 5°N. Although there appeared to be other cruises that occupied this line, we used the data from the selected three cruises because the water property measurements, including total carbon and oxygen, were available from the Climate and Ocean Variability, Predictability and Change (CLIVAR) and Carbon Hydrographic Data Office.

To show the difference in measurements between the cruises, we interpolated the data on grids with a vertical interval of 2 dbar

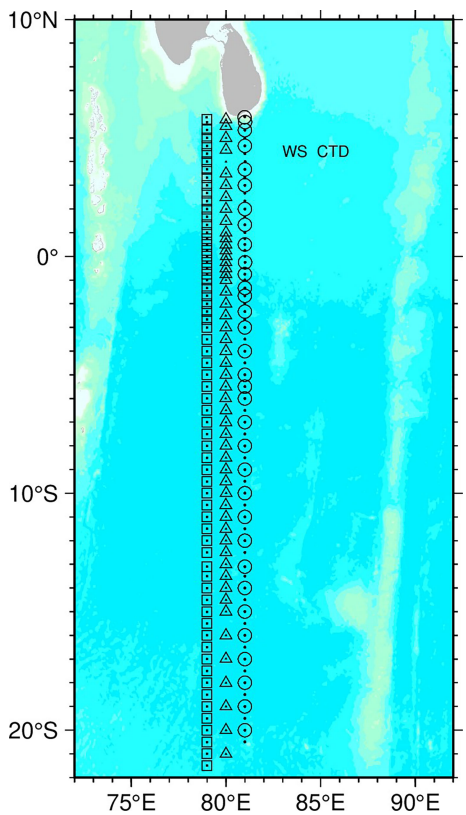

FIGURE 1 | Observation stations along 80°E (I08N) that were used in this study. We used three sections that were occupied in March (316N14_7 by R/V Knorr; Swift and Becker, 2019a), September 1995 (3175MB95_07 by R/V_Malcolm Baldrige; Swift and Becker, 2019b), and December 2019. The stations in March 1995 and December 2019 are shifted to 1° west and east, respectively.

and horizontal intervals of 0.25° using the Akima spline. We calculated the neutral densities (γ) based on the gridded datasets of the vertical sections and set the water properties on the isopycnal surfaces to investigate water property changes without the strong effects of isopycnal heaving.

Changes in anthropogenic carbon (C_{anth}) were estimated using a method similar to that used in a previous study (Kouketsu et al., 2013, Appendix). We calculated the anthropogenic increases based on both isopycnal and isobar surfaces to show the isopycnal heaving effects on the estimations.

Argo Gridded Dataset

We used a gridded dataset based on the Argo array to compare the long-term and seasonal variability of salinity with changes revealed by the GO-SHIP sections. The dataset was obtained *via* objective mapping methods of neutral density, similar to the one used by Kouketsu et al. (2017) based on recent profile data (Argo, 2021), and is the monthly 1°×1°×0.05γ gridded data of salinity, temperature, and isopycnal depths from 2000 to 2020. Based on this gridded data and isobaric dataset of the grid point value of the monthly objective analysis (Hosoda et al., 2008), we calculated the monthly geostrophic velocity with approximate stream functions (McDougall and Klocker, 2010). The detailed methods to produce the gridded dataset including in geostrophic velocity calculations were described in Kouketsu et al. (2017). In this study, the salinity anomalies were calculated from the monthly climatology, which was calculated by averaging the monthly data over the period of 2006–2020.

RESULTS

Changes Along the Section

In 2019, a large decrease in salinity (< -0.2) compared to that in 1995 was broadly observed in the subsurface layers (50–250 dbar in **Figure 2**; changes in the intermediate layers are shown in **Figure S2 in the Supplement**). In particular, large salinity decreases were detected at approximately 100 dbar below the mixed layers from 15°S to 2°S. In one part of the area of the salinity decrease detected south of the equator, relatively large increases in dissolved oxygen (DO; > 30 μmol kg^{-1}) and decreases in nitrate (< -4 μmol kg^{-1}) and dissolved inorganic carbon (DIC; < -50 μmol kg^{-1}) were also detected, whereas the opposite changes (decrease of DO and increase of nitrate and DIC) were detected both in the lower part associated with salinity decreases (150–300 dbar in **Figure 2**) and north of the equator, at around 100 dbar. Although the DIC near the surface layers

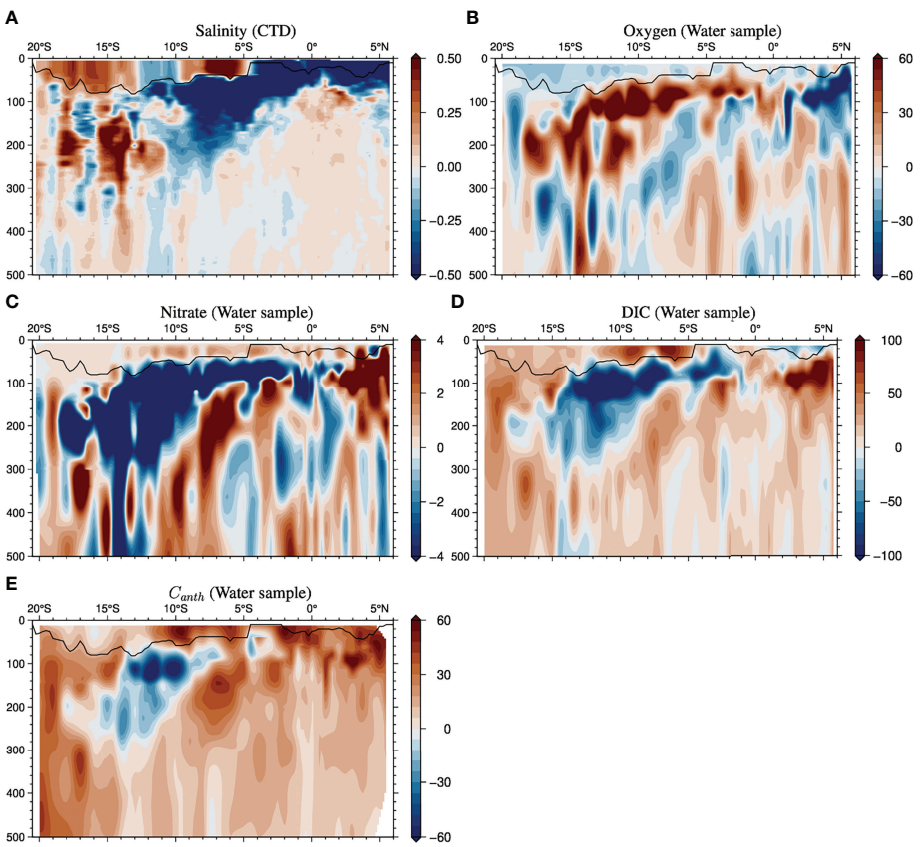

FIGURE 2 | Changes (from September 1995 to December 2019) in salinity **(A)**, DO **(B)**, nitrate **(C)**, DIC **(D)** and anthropogenic carbon **(E)** on isobar surfaces along the 80°E section (**Figure 1**). Mixed layer depths, where the densities were denser than 0.125 kg m^{-3} at 10 dbar, are shown with black lines.

generally tended to increase with the increase in C_{anth} in the atmosphere, large decreases in DIC at approximately 100 dbar south of the equator were detected just below the mixed layer, revealing its strong effect of natural changes on the distribution of water properties. Furthermore, large nitrate changes below the mixed layers were also detected, which might affect biological productivity in the surface through subsurface layer vertical mixing, as well as around the bottom of the euphotic layers where the chlorophyll maximum is frequently observed.

On the isopycnal surfaces around 100 dbar from 15°S to 2°S, nitrate and DIC increased (~4 and ~50 μmol kg^{-1}, respectively), and DO decreased (-30 μmol kg^{-1}) (**Figures 3** and **S3 in the Supplement**), which were opposite to the results based on the comparison of isobar surfaces (**Figure 2**). Although changes in the advection and isopycnal mixing seemed to be the potential cause of the decreases in DO, as well as the increases in nitrate and DIC, comparison of the isobar surfaces in this region showed that the isopycnal heaving was too large to have exhibited the opposite changes. In fact, large increases in isopycnal depths (30–60 dbar were observed just below the mixed layers (**Figure 3F**). Such a strong heaving effect also potentially caused the apparent decrease of C_{anth} according to the comparison of isobar surfaces, the features of which disappeared in the analysis of the isopycnal surfaces (**Figure 3E**). As the vertical gradient amplitude of salinity was relatively small compared with the effects of advection changes on isopycnal surfaces and those of DO, nitrate, and DIC were large (**Figures 4** and **S4 in the Supplement**), the reverse of the changes between the isobar and isopycnal surfaces did not occur in salinity. Below approximately 150 dbar, the patterns (and magnitudes) of the water property changes on the isobar surfaces (**Figures 2A–D**) were strongly similar to those on the isopycnal surfaces (**Figures 3A–D**), whereas the relatively large heaving at approximately 12°S and 8°S (**Figure 3E**) seemed to be the potential cause of a slight decrease (increase) and increase (decrease) in DIC (DO) at a depth of approximately 500 dbar (**Figures 2B, D**).

As the dissolved chemical properties were not frequently observed in this section, we did not know the details of their variability. However, the salinity and temperature observational data were sufficient to capture the monthly variability owing to the Argo array. In the next subsection, we compare the anomalies of salinity from the long-term mean with the salinity changes based on the GO-SHIP sections to assess the changes in detail.

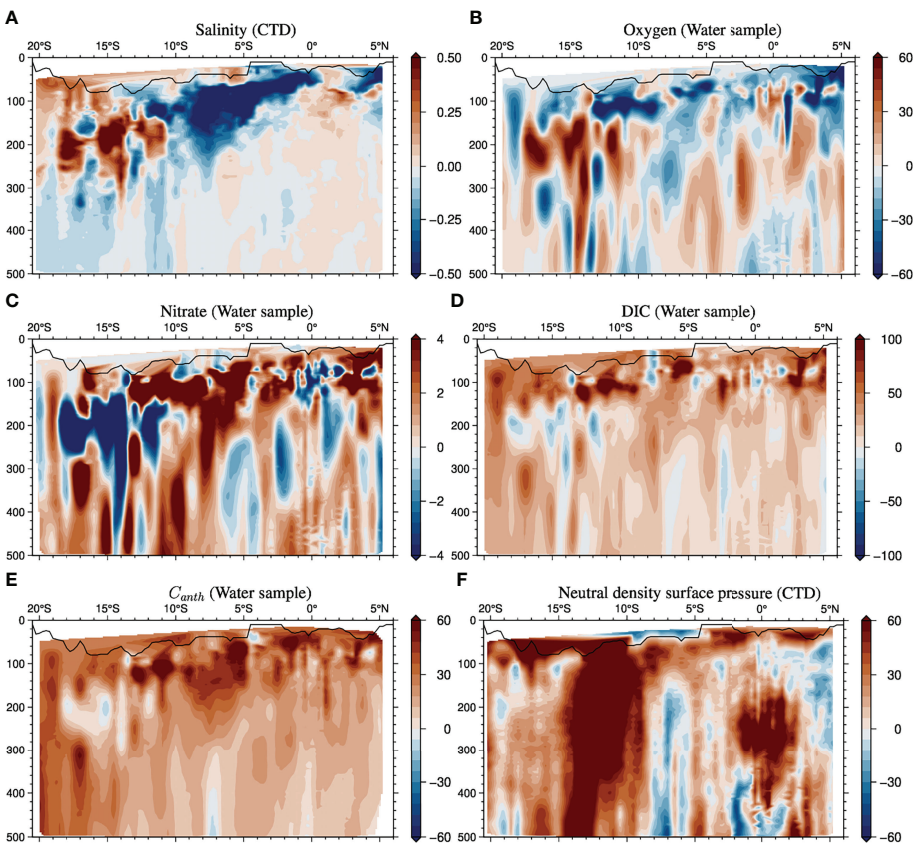

FIGURE 3 | Same as **Figures 2A–E**, but for changes (from September 1995 to December 2019) on isopycnal surfaces. The changes in isopycnal surface depth is shown in **(F)**. To project the changes on isopycnal surfaces to isobar surfaces, the mean isopycnal surface depths in two cruises (September 1995 and December 2019) were used. Mixed layer depths defined as those with densities denser than 0.125 kg m^{-3} at 10 dbar, are shown with black lines.

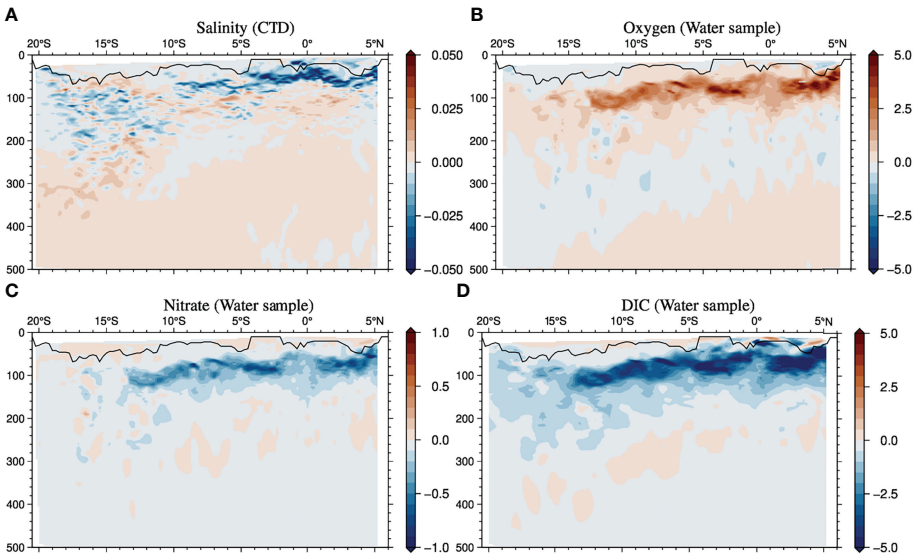

FIGURE 4 | Vertical gradient of mean salinity **(A)**, DO **(B)**, nitrate **(C)**, and DIC **(D)** in September 1995 and December 2019.

Comparison of Salinity Change Patterns With the Temporal Changes Appearing in the Gridded Data

The clear decreases in interannual salinity (approximately -0.5) were estimated at approximately 100–200 dbar from 15°S to 5°N (**Figure 5A** and see **Figure S5 in the Supplement**) in December 2019 with the gridded data based on the Argo float array. As the salinity decreases were similar to those on the isopycnal surfaces (**Figure 5C**), the anomalies were likely mainly caused by advection and mixing changes on the isopycnal surfaces rather than by isopycnal heavings associated with Rossby wave propagations. The decreases were also similar to the differences observed in 2019 from 1995 (**Figures 2A** and **3A**). Therefore, the decrease in salinity revealed by the comparison of the two

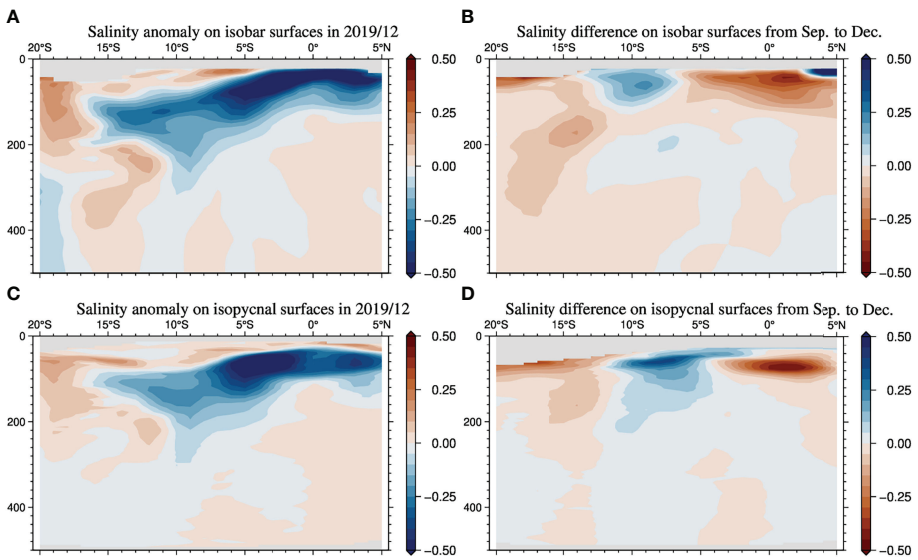

FIGURE 5 | Salinity anomalies on the isopycnal surfaces **(A)** and isobar surfaces **(C)** from monthly climatology (averaged over 2006–2020) along 80°E based on the Argo gridded dataset and differences in the climatological salinity based on the gridded dataset from September to December on the isopycnal **(B)** and isobar surfaces **(D)**.

sections strongly reflected the interannual changes in ocean circulation, whereas the seasonal changes may have contributed (**Figures 5B, D**) to the actual changes. The temporal development of this salinity anomaly was captured in the horizontal map of salinity anomalies on the isopycnal surface of 25.0γ (**Figure 6**), which was located at approximately 150 dbar (see **Supplement 9.1**), where strong salinity decreases were observed (**Figures 2A** and **3A**). The low-salinity anomaly formed around 10°–5°S, 90°E between August and October 2019, associated with the westward current anomalies around 5°S, 90°E (**Figures 6A, B**). The pIOD, which tends to cause strong upwelling and low-salinity anomalies around the region of 100°E, amply developed in 2019 and this was one of the strongest pIOD events since 2000. The low-salinity anomaly associated with the strong pIOD seemed to extend to 80°E by the westward current anomalies around 5°S, 70°–90°E in December (**Figure 6C**) when the mode was slightly attenuated (**Figure 7B**). Furthermore, a low-salinity anomaly was observed around February 2020, whereas the positive dipole mode ceased (**Figure 6D**). Therefore, the current anomalies forming the salinity anomalies can be associated with isopycnal heaving (**Figure 8**) due to Rossby wave propagation. The westward current anomalies around 5°S, 70°–90°E, which seemed to contribute to extending the low-salinity anomalies (**Figures 6B, C**), were observed in the region between the occurrence of shallow (around 5°S, 90°–100°E) and deep-isopycnal anomalies (around 10°S, 60°–80°E; **Figures 8B, C**). Particularly, the shallow isopycnal anomalies around 5°S, 90°–100°E were associated with upwelling associated with pIOD. The low-salinity anomalies were also distributed south of 5°S in December 2019 (**Figure 6C**), and deep-isopycnal anomalies were observed (**Figure 8C**), causing the suppression of changes on isopycnal surfaces (**Figures 3B, C**) from those on isobar surfaces (**Figures 2B, C**). As the time series of the salinity changes at 5°S, 80°E in the subsurface layers (**Figure 7A**) could be correlated with the dipole mode index (DMI), it can be stated that the salinity changes as well as the isopycnal depths along 80° E were significantly correlated with the DMI with 2–8 month lags (**Figure 9**). As the significant positive correlation of isopycnal depths at approximately 15°S–5°S (**Figure 9B**) was associated with the negative correlation of salinities (**Figure 9A**), this suggests that the induced low-salinity anomalies associated with pIOD and strong effects of heaving on biogeochemical properties could be a common phenomenon. It should be noted that significant correlations with isopycnal surface depths and salinity anomalies were detected in the deeper layers as well as in the surface layers (**Figure 10**), and their patterns were similar to the differences between the two cruises (**Figures 3A, E**), suggesting that the differences between the two cruises could be reflective of the changes caused by the pIOD.

The low-salinity anomaly observed in 2019 is the clearest anomaly captured by the Argo observation network after 2006. Although a similar pIOD event also occurred in 1994, that event ceased in December 1994 (**Figure 8A**). Despite considering the lag due to propagation towards 80°E, the influence of the event on subsurface salinity anomalies was unclear in September 1995. Therefore, the subsurface changes between 1994 and 2019 reflect the influence of the positive dipole mode event (**Figure 8B**).

The gridded data from the observational sections showed small differences among the changes in terms of the strong salinity decrease. The amplitudes of the changes in the salinity increases at depths of 200–400 dbar at approximately 15°S and near 150 dbar at approximately 0°, as well as the significant decreases at approximately 100–200 dbar (**Figures 5A, C**), were

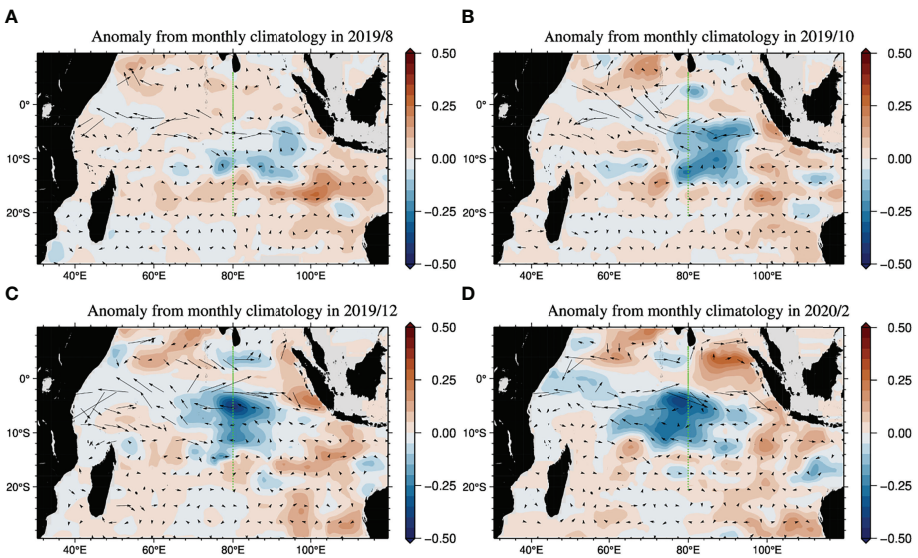

FIGURE 6 | Salinity anomalies in August 2019 **(A)**, October 2019 **(B)**, December 2019 **(C)**, and February 2020 **(D)** from the climatological mean (2006–2020) at 25.0γ based on the Argo gridded dataset. The black arrows show the geostrophic velocities at 25.0γ. The green dots show the stations along the I08N line in 2019.

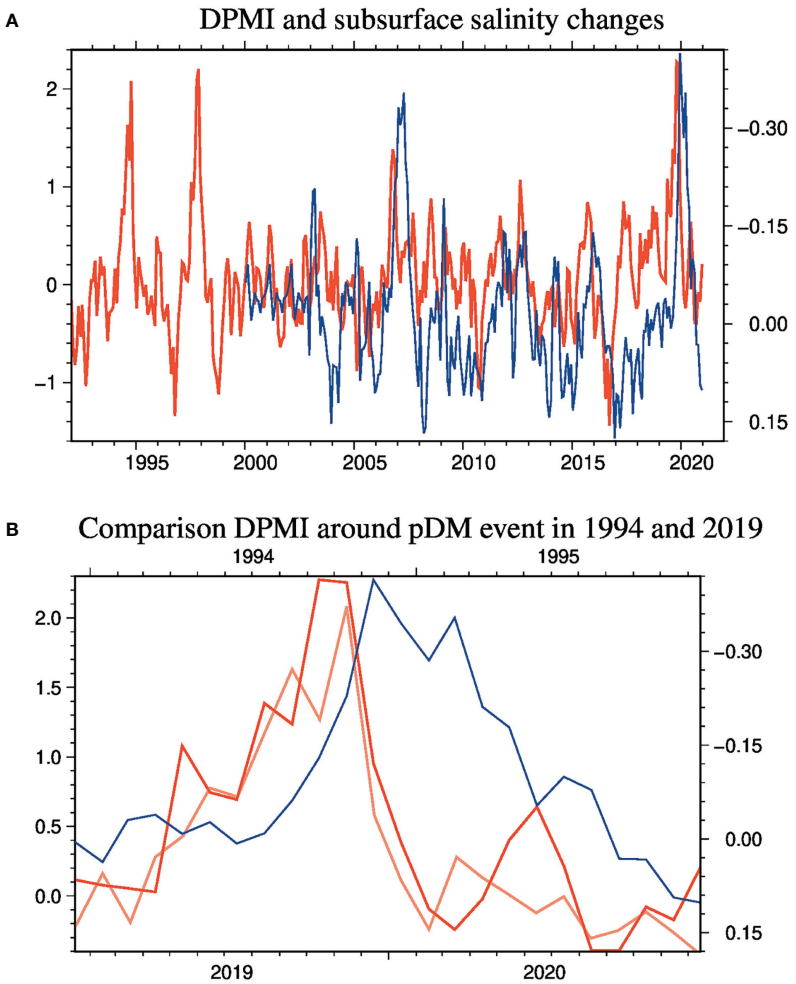

FIGURE 7 | Dipole mode index (DMI; red) and salinity (blue) variabilities in the subsurface layers (25.0γ) at 5°S, 80°E from 1992 to 2000 **(A)** and comparison of the temporal changes in DMI (red) and salinity (blue) during the pIOD in 2019 with those in DMI (pink) during the pIOD in 1994 **(B)**. The temporal changes in salinity were based on the Argo gridded dataset. DMI is defined as the SST anomaly difference between the regions of 50°E–70°E, 10°S–10°N and 90°E–110°E, 10°S–0° (Saji et al., 1999) based on NOAA OI SSTv2 (Reynolds et al., 2002).

smaller than those observed in the GO-SHIP sections (**Figures 2A** and **3A**). The difference between the long-term mean for December and September could elucidate these changes, especially for increases ranging within approximately 200–400 dbar near 15°S and at 150 dbar near the equator, and decreases ranging within approximately 100–200 dbar between 15°–10°S (**Figures 5B, D**). These differences between the gridded data and the observational sections could be caused by differences between the observational section in 1995 and the climatology based on gridded data, as well as more short-term (mainly < 1 month) variabilities.

Effect of Isopycnal Heaving on Biogeochemical Properties

The salinity changes appearing in the comparison with the GO-SHIP sections could be strongly influenced by large interannual changes associated with the pIOD event and relatively small seasonal changes. These changes seemed to have been caused by ocean circulation changes on the isopycnal surfaces. The changes in other dissolved materials on the isopycnal surfaces may also have been influenced by dipole events. The decreases in DO and increases in nitrate and DIC (**Figure 3**) in the lower part of the salinity decreases (150–250 dbar from 10°S–0°) are consistent with the broad extension of low-DO and nutrient-rich deeper waters from the eastern upwelling regions. In the upper part of the region of salinity decreases (around 100 dbar below the mixed layers), the changes in DO and nitrate seemed to be strongly influenced by the isopycnal heavings because of the greater vertical gradients (**Figure 4**). Although advection (and mixing) might draw low-DO and nutrient-rich waters to the region below the mixed layers, the strong isopycnal depression appears to have caused a nutrient decrease, especially from 15°–5°S. We assessed the vertical heaving effect associated with interannual and seasonal changes with isopycnal depth

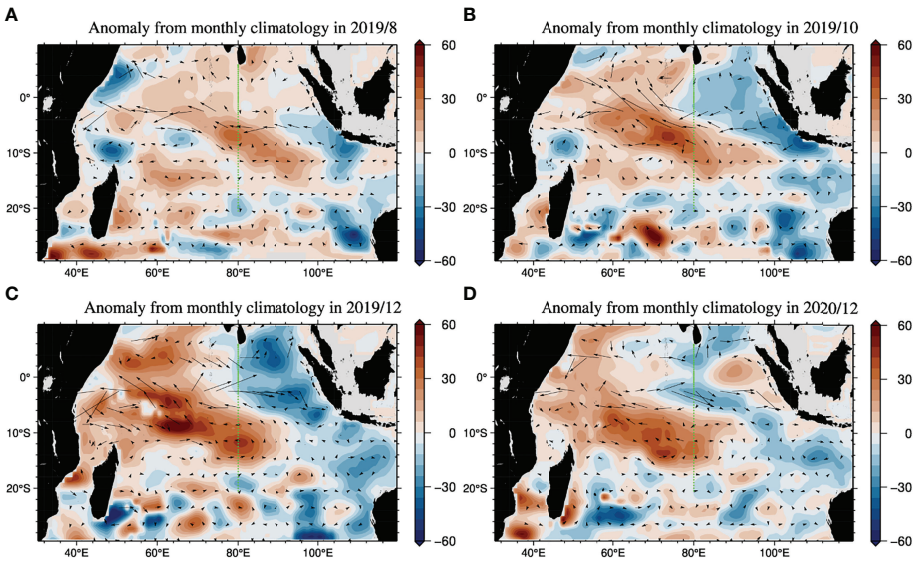

FIGURE 8 | Pressure anomalies in August 2019 **(A)**, October 2019 **(B)**, December 2019 **(C)**, and February 2020 **(D)**. The black arrows show the geostrophic velocities at 25.0γ. The green dots show the stations along I08N line in 2019.

changes revealed by the Argo gridded data, assuming that the distributions of DO and nitrate on isopycnal surfaces in 2019 were similar to the long-term mean ones along the GO-SHIP vertical sections (**Figure 11** and see **Figure S6**). The effects of the interannual changes in isopycnal depths were inferred to be a 60 μmol kg^{-1} increase of DO and a -4 μmol kg^{-1} decrease of nitrate below the mixed layers from 15°S–0°, respectively, whereas the effects of the seasonal changes were clear around 10°S. The large increase of DO and decrease of nitrate below the mixed layer (**Figure 2**) might be strongly influenced by interannual isopycnal depth changes associated with the pIOD, whereas the influences of the seasonal isopycnal depth changes seemed to be relatively large in comparison with the ones in salinity (**Figures 5** and **11**).

Isopycnal heaving likely affected the water column inventory changes in anthropogenic and natural carbon (**Table 1**). Although the water-column natural carbon changes estimated

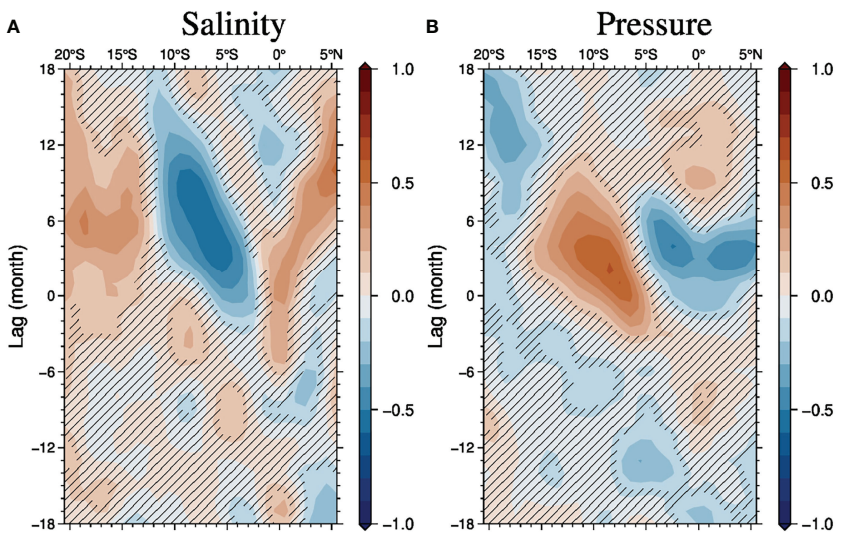

FIGURE 9 | Lead-lag correlations of salinity **(A)** and isopycnal depth **(B)** with DMI (**Figure 7**) on 25.0γ along 80°E based on the Argo gridded dataset. The non-hatched areas correspond to areas of high significance (p-value <0.1).

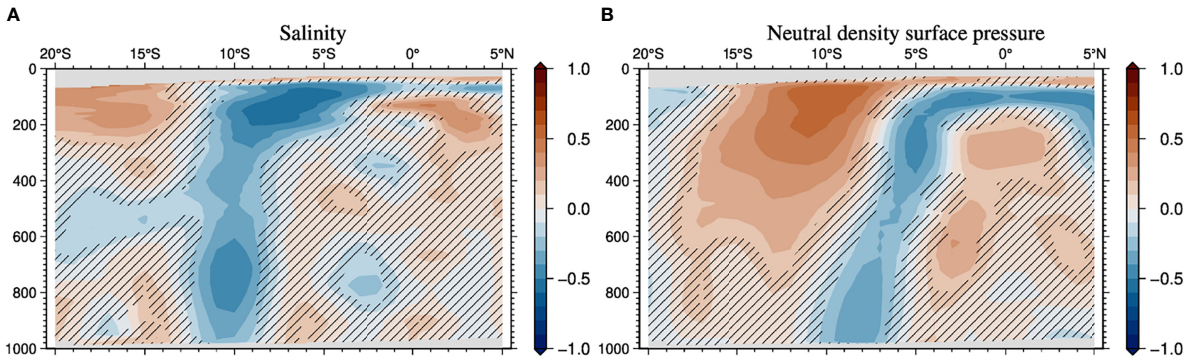

FIGURE 10 | Four-month-lag correlations of salinity **(A)** and isopycnal depths **(B)** with DMI (**Figure 7**) in the vertical section along 80°E based on the Argo gridded dataset. The non-hatched areas corresponded to areas of high significance (p-value < 0.1).

with those in DO on the isopycnal surfaces were insignificant, large effects were estimated in the comparison of the isobar surfaces from 15°S–10°S, where the increase in anthropogenic carbon was estimated to be small on the isobar surfaces owing to large downward isopycnal heaving in this region. These differences between the isopycnal and isobar surfaces are an example of the effects of physical changes on the distribution of carbon.

The changes in water-column inventories (16–28 mol m^{-2}) based on the isopycnal surfaces corresponded to 0.6–1.1 mol m^{-2} yr^{-1}, and compared with the 1995 and 2007 GO-SHIP type sections, were slightly larger than those estimated along 90°E (Kouketsu and Murata, 2014). This might reflect the recent (since 2007) increase in CO_2 concentration in the atmosphere, whereas quantitative ocean absorption increases remain unclear. However, as the changes in water properties on the isopycnal surfaces also appeared to be influenced by seasonal changes as well as the pIOD event, additional in-depth surveys and comparisons with numerical models are needed to quantitatively assess the detailed changes.

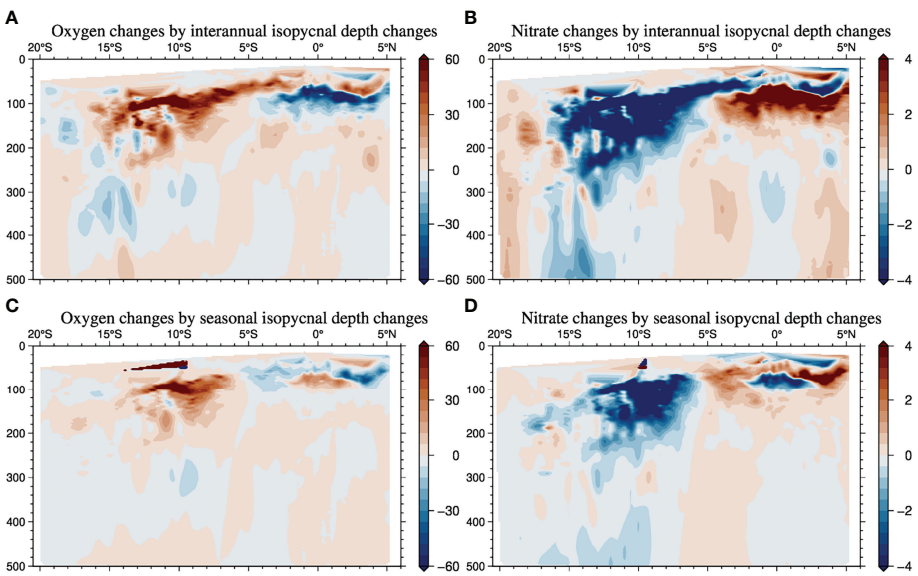

FIGURE 11 | Effects of the interannual isopycnal depth anomalies on the changes in DO **(A)** and nitrate **(B)** in December 2019 and effects of the seasonal isopycnal depth anomalies on the changes in DO **(C)** and nitrate **(D)** in December from the annual mean. The effects were estimated by multiplying the anomalies (from the monthly climatology and annual mean which are calculated monthly gridded data in 2006–2020) in interannual and seasonal isopycnal depths calculated with the Argo gridded dataset (ex. interannual anomalies are shown in **Figure 8**) by the vertical gradient of DO and nitrate (**Figure 4**), assuming that long-term mean distributions of DO and nitrate on isopycnal surfaces were similar to those obtained by the cruise in 2019.

TABLE 1 | Water-column storage changes above 3000 dbar in anthropogenic (C_{ant}) and natural (C_{aou}) carbons (mol m^{-2}) from 1995 to 2019 based on property comparisons of isopycnal and isobar surfaces. .

Area		20°S–15°S	15°S–10°S	10°S–5°S	5°S–0°	0°–5°N
Isopycnal	C_{ant}	28 ± 3	21 ± 4	16 ± 3	16 ± 3	19 ± 3
	C_{aou}	2 ± 3	1 ± 4	-1 ± 4	-1 ± 4	3 ± 4
Isobar	C_{ant}	21 ± 4	4 ± 5	13 ± 4	12 ± 4	16 ± 4
	C_{aou}	-2 ± 5	-13 ± 5	-4 ± 5	-1 ± 5	4 ± 5

SUMMARY AND DISCUSSION

We conducted this study in the meridional section along 80°E utilizing highly accurate observational data of numerous variables to elucidate circulation and its changes in the Indian Ocean. By comparing cruises in 2019 and 1995 on isobar surfaces, clear salinity decreases at approximately 100–300 dbar were observed. The salinity decreases on the isobar surfaces were quite similar to those on the isopycnal surfaces, while the contribution of vertical advection (isopycnal surface heaving) to the salinity changes seemed to be limited just below the mixed layer (around 50 dbar in **Figures S2** and **S3 in the supplement**) near the equatorial regions (5°S–5°N), which was consistent with a previous study (Kido and Tozuka, 2017). Thus, the salinity changes below the mixed layers were mainly formed by anomalous advection and mixing on the isopycnal surfaces. To infer contributions to salinity anomalies on isopycnal surfaces of the advection effects, we integrated the advection of long-term mean (2006–2020) monthly salinity distributions with interannual currents from August to December in 2019 (**Figure 12A**). The interannual anomalous currents were found to be representative of monthly anomalies in the currents from the long-term climatological mean (2006–2020). The effect of the

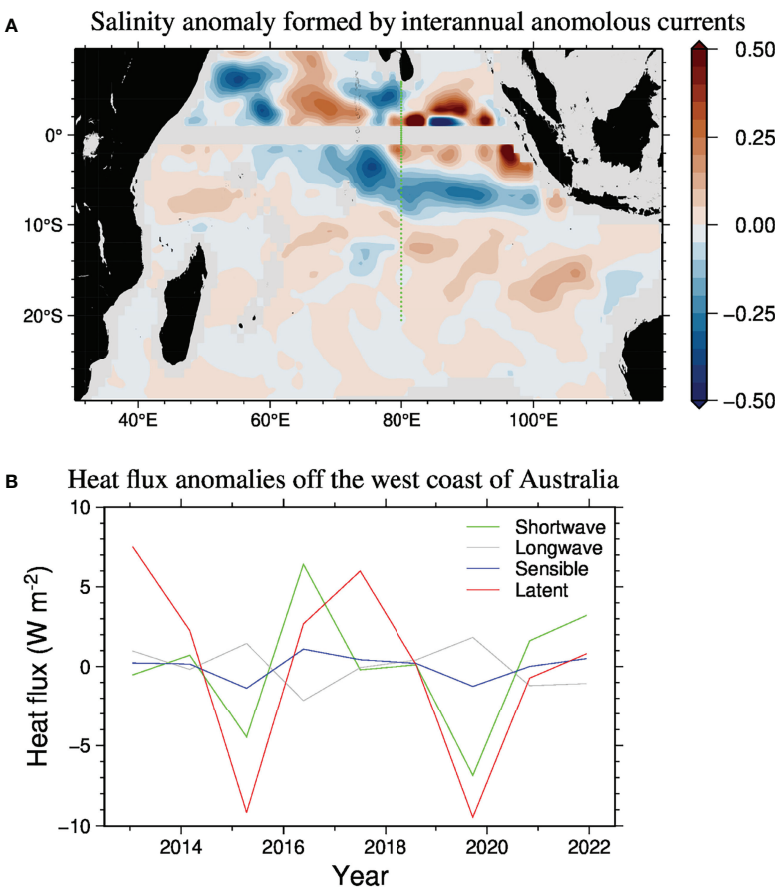

FIGURE 12 | **(A)** Estimated salinity anomalies on 25.0γ based on the Argo gridded dataset, which could be formed by interannual seasonal anomalous currents from August 2019 to December 2019. **(B)** Annual-mean surface heat flux anomalies averaged over 15°-27.5°S, 80°-115°E from the long-term mean (2013-2021) for shortwave radiation (green), longwave radiation (gray), sensible heat flux (blue), and latent heat flux (red), based on ERA5 data (Hersbach et al., 2019).

interannual anomalous advections seemed to reveal the actual salinity decrease around 5°S, 80°E (**Figures 6C**), while the other advection effects (ex. advection with interannual salinity changes and anomalous currents) were not so large (not shown). This suggests that the interannual anomalous geostrophic velocity changes were dominant for subsurface salinity changes around 5° S, 80°E, though the isopycnal mixing could not be explicitly estimated. The advection effects (**Figure 12A**) were confined around the eastern part of the equatorial Indian Ocean, and corresponded to the edge of the negative pressure anomaly tongue around 80°E–100°E and 5°S, which were formed in association with the pIOD (**Figure 8C**). Based on the long-term gridded dataset obtained using the Argo float array, the interannual anomalies (rather than the seasonal anomalies) were dominant in forming the changes along the sections, particularly north of 10°S. The importance of forming subsurface salinity anomalies associated with the IOD revealed by the analysis is consistent with findings of a previous analysis based on historical IOD events (Kido et al., 2019). This study was regarded as a case study corresponding to super-strong period events and based on trans-basin observations. The negative salinity anomalies south of 10°S were unlikely to have been formed by the interannual anomalous currents (**Figure 12A**), and seemed to reflect more long-term changes, as the negative changes around 12°S along 80°E in August 2019 (**Figure 6A**) have been observed before (not shown). This finding is consistent with those regarding longer-term westward propagation of salinity anomalies around 12°S, formed off the west coast of Australia, as shown in a previous study (Nagura and Kouketsu, 2018). As that study showed that negative salinity anomalies are generally formed by the changes in positive surface heat flux from the atmosphere to the ocean off the west coast of the Australia (with 1–2yr lags), the salinity decrease observed in this study might correspond to the water mass modification associated with warming conditions for 2016–2018 (**Figure 12B**). As salinity advection changes in the ITF have also contributed to form salinity changes around 12°S on interannual time scales (Hu et al., 2019), broader analysis is needed to clarify the detailed contribution of these salinity changes.

In addition to the changes in salinity, we report changes in other water properties of DO, nitrate, and DIC. On the isopycnal surfaces, the decreases in DO and increases in nitrate and DIC were observed in the area where salinity decreased, suggesting that the nutrient-rich, low-DO, and low-salinity water extended to the west by westward flows in the latter half of the pIOD event period. However, for the changes in biogeochemical variables, isopycnal heaving seemed to be more important than changes in salinity. Particularly, around the upper part of the salinity decreases (approximately 100 dbar), the opposite changes of DO (increase), nitrate, and DIC (decreases) were observed on the isobar surfaces, where the vertical gradient of the biogeochemical variables just below the mixed layers and heaving associated with the pIOD event were too large to clearly show the effect of the horizontal advection, and the downward heaving suppressed the increases in nutrients. This might explain why chlorophyll-a increases were limited to the narrow region in the eastern part near the equatorial region in the biological IOD (Shi and Wang, 2021). In addition, the heaving effect seemed to cause apparent changes in anthropogenic carbon estimations, particularly in the region of 10°S–15°S, which was far away from the enhanced upwelling associated with the pIOD, and thus heaving may not have been caused by the direct influence of the pIOD. As the changes in salinity in the subsurface layers around 100–300 dbar north of 10°S were strongly influenced by interannual anomalous currents, the changes in biogeochemical material distribution in this region might have been associated with the pIOD. The salinity changes south of 10°S seemed to be related with the changes in the ITF (Hu et al., 2019), as well as water mass formations (Nagura and Kouketsu, 2018), which could also have caused the noted changes in biogeochemical material distribution. However, the distribution of biogeochemical materials was different from that of salinity, and thus it might be difficult to estimate the biogeochemical material distribution in detail due to sparse observations. Note that the seasonal changes on the isopycnal surfaces could have influenced the biogeochemical property changes more strongly than could salinity, due to biological activity changes as well as advection and diffusion changes. In the future, quantitative evaluations will be performed with more intensive observations utilizing an Argo float with biogeochemical sensors.

Although the DIC decrease below the mixed layers was also observed on the isobar surfaces, relatively large increases in DIC were observed on the sea surface at approximately 10°S, which was consistent with the relationship between DIC changes and the IOD based on previous numerical simulations (Valsala et al., 2020). Horizontal advection might be more important for the simultaneous formation of positive DIC anomalies on the surface in the pIOD than vertical mixing at the bottom of the mixed layers at 80°E. As nutrient- and DIC-rich waters were broadly distributed on the isopycnal surfaces, the effect of the elevated DIC value formed by horizontal advection might have appeared clearly after the deep isopycnal depth anomalies passed, which could have also affected biological activity due to the relatively high nitrate in the subsurface layers. The low-salinity anomalies, which could be associated with high DIC and nutrients, tended to remain for longer periods than the isopycnal depth anomalies (**Figure 9**).

We inferred the relationship between subsurface changes and pIOD by comparing two observations only, since the available observations were limited. Considering this, the time series of salinity changes based on the gridded database we found to support the interpretations, at least for salinity change. In the future, the effects of IOD on biogeochemical cycles will be assessed more accurately and involve in-depth observations and comparison with numerical simulations.

The patterns of the changes between September 1995 and December 2019 were quite similar to those between March 1995 and December 2019 (**Figures 13** and **14**; corresponding changes in the intermediate layers are shown in **Figures S7** and **S8 in the Supplement**). The cruise period of March 1995 occurred immediately after the pIOD event in 1994. Low-salinity waters remained in the subsurface layers, assuming that the temporal changes were the same as the pIOD in 2019. However, the observed decrease in salinity was also clearly detected, as in the comparison with September, which may be an indication of differences between the events depending on their strengths. However, more detailed assessment including seasonal changes is needed to assess such differences of the IOD strengths.

Whole changes through the Indian Ocean associated with the IOD and are unclear in this study. Particularly, changes in the mixed layers were not described because we focused on the changes revealed only by the ship observations, which could not capture high-frequency changes in the mixed layers, and we compared the changes with continuous monitoring by the Argo float array. Although the contributions associated with seasonal changes were not so large (except around 50–80 dbar just below the mixed layer) in the subsurface layers along 80°E (e.g., **Figures 5B, D**), analyses focusing on the effects of the changes in the mixed layers and vertical diffusivity as well as geostrophic advections will be needed to evaluate detailed seasonal changes. Furthermore, as the salinity changes shown in this study were similar to those reported in previous studies (e.g., Li and Wang, 2015; Nagura and Kouketsu, 2018), the interannual changes seemed to be relatively clear when compared with the longer-term changes. However, as such long-term changes might be associated with global warming, freshwater flux changes, or long-term natural variations in the ocean surface near Southern ocean, especially in the deeper layers corresponding to Subantarctic Mode Water and Antarctic Intermediate Water (e.g., Bindoff and Mcdougall, 1994; Bryden et al., 2003; Durack and Wijffels, 2010; Kobayashi et al., 2012), more detailed analyses and comparison with biogeochemical property changes are needed in the future, requiring broader observations in the Southern Ocean as well as the southern part of the subtropical region in the Indian Ocean.

In this study, we highlight changes in the dissolved materials in the upper layers (above 500 dbar) to focus on the direct effects of the pIOD event. However, we also find that the correlation between these changes and the DMI seems to

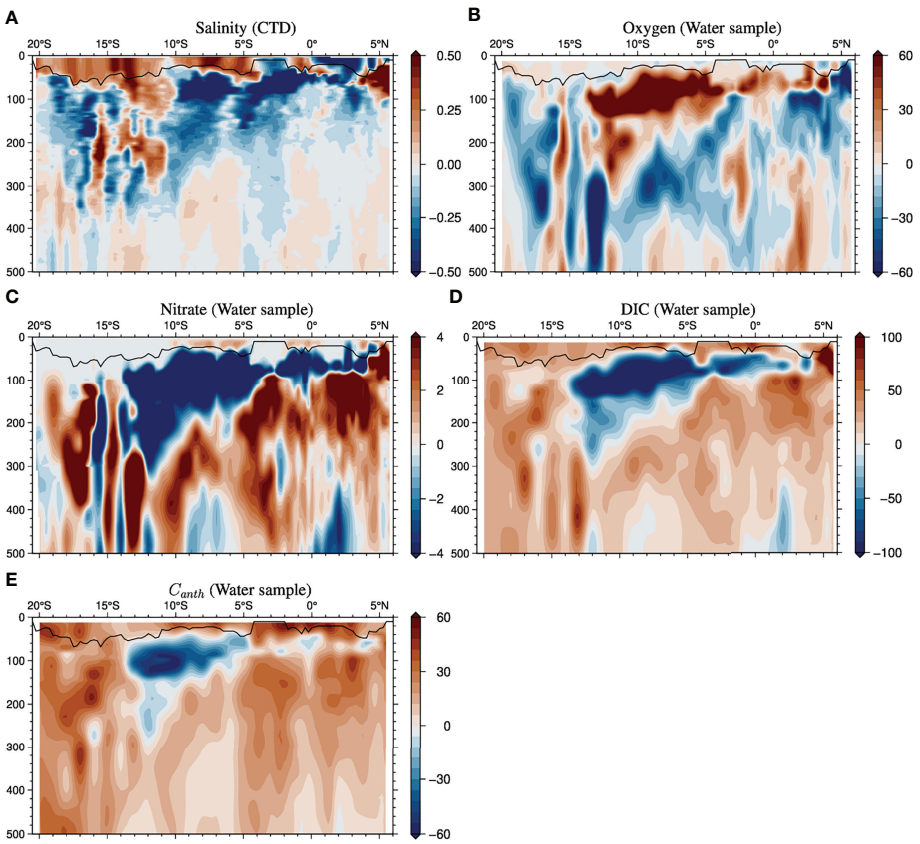

FIGURE 13 | Same as **Figure 2** but for the changes from March 1995 to December 2019.

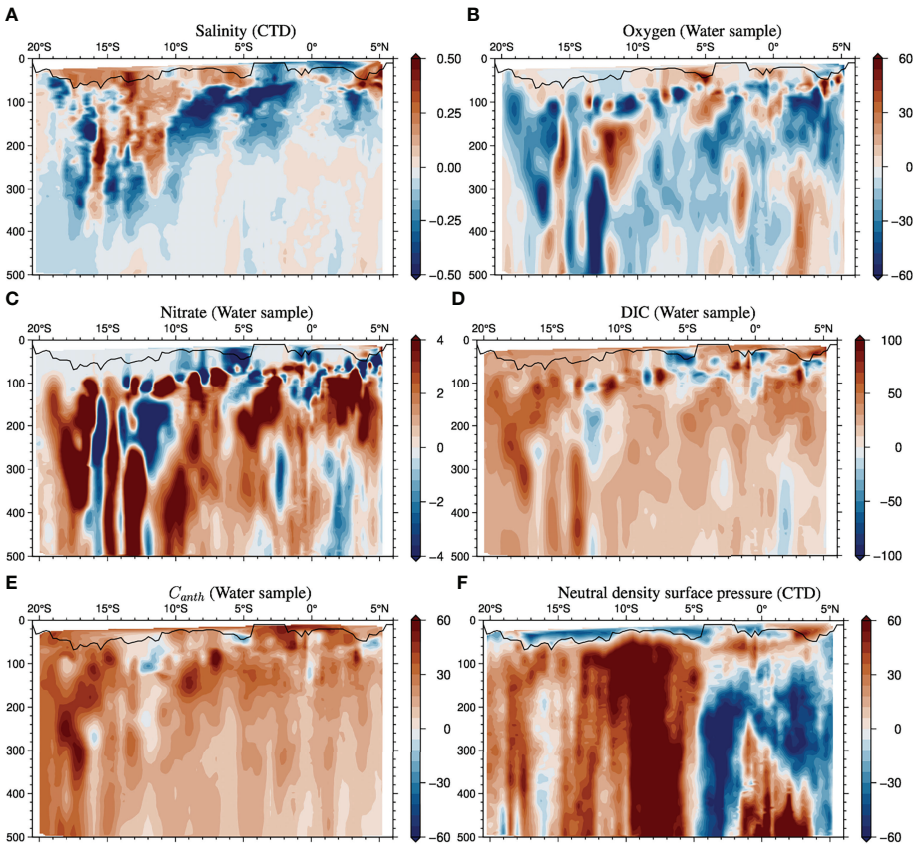

FIGURE 14 | Same as **Figure 3** except for the changes from March 1995 to December 2019, changes in salinity **(A)**, DO **(B)**, DIC **(C)**, anthropogenic carbon **(D)**, and isopycnal depth **(F)**.

be significant in some regions of the deeper layers (around 800 dbar at 5°S in **Figure 10**), though the amplitude of the changes in the deeper layers was quite small (**Figure S5**). To assess the influence of IOD events in the deeper layers in future research, more careful investigation is required, particularly focusing on changes according to the Argo float measurements. Furthermore, changes in the deep layers (below 1000 dbar) may be related with other effects not focused on in this study (ex. associated with the bottom water changes reported by Kouketsu et al., 2011). In future research, we will report recent changes in the deeper layers of the Indian Ocean, including those associated with the phenomena revealed by this study.

DATA AVAILABILITY STATEMENT

The datasets presented in this study can be found in online repositories. The names of the repository/repositories and accession number(s) can be found below: http://www.esrl.noaa.gov/psd/data/, https://doi.org/10.17882/42182#80076, http://www.jamstec.go.jp/ARGO/J_ARGOe.html, https://cchdo.ucsd.edu.

AUTHOR CONTRIBUTIONS

SK analyzed changes in water properties along the section and wrote the main contents. AM supported analyzing DIC and anthropogenic carbon changes and changes in mixed layers for discussion. KA supported observation near of Sri Lanka. All authors contributed to the article and approved the submitted version.

FUNDING

This work was supported by KAKENHI, Grant JP18H04129.

ACKNOWLEDGMENTS

The author thanks the captain, crews, and researchers on the Indian Ocean cruise in 2019 by the R/V Mirai. We also appreciate the efforts made to reinforce the observation networks under GO-SHIP and Argo. We thank Drs. T. Doi

and T. Horii for their useful comments on this work. We also thank the editor and the reviewers for comments on earlier version of this paper. The NOAA High Resolution SST data are provided by NOAA/OAR/ESRL PSL, Boulder, Colorado, USA, from their website (http://www.esrl.noaa.gov/psd/data/). The surface heat fluxes were provided by Copernicus Climate Change Service information, and were modified. Neither the European Commission nor ECMWF is responsible for any use that may be made of the Copernicus information or data it contains. We would like to thank Editage (www.editage.com) for English language editing.

SUPPLEMENTARY MATERIAL

The Supplementary Material for this article can be found online at: https://www.frontiersin.org/articles/10.3389/fmars.2022.848756/full#supplementary-material

REFERENCES

Anderson, L. A. L. A., and Sarmiento, J. L. J. L. (1994). Redfield Ratios of Remineralization Determined by Nutrient Data Analysis. *Global Biogeochem. Cycle.* 8 (1), 65–80. doi: 10.1029/93GB03318

Argo (2021). Argo Float Data and Metadata From Global Data Assembly Centre (Argo GDAC) - Snapshot of Argo GDAC of January 10st 2021. *SEANOE*. doi: 10.17882/42182#80076

Bindoff, N. L., and Mcdougall, T. J. (1994). Diagnosing Climate Change and Ocean Ventilation Using Hydrographic Data. *J. Phys. Oceanogr.* 24 (6), 1137–1152. doi: 10.1175/1520-0485(1994)024<1137:DCCAOV>2.0.CO;2

Bryden, H. L., McDonagh, E. L., and King, B. A. (2003). Changes in Ocean Water Mass Properties : Changes Inocean Water Mass Properties : Oscillations or Trends? *Science* 300 (2003), 2086–2088. doi: 10.1126/science.1083980

Doi, T., Behera, S. K., and Yamagata, T. (2020a). Predictability of the Super IOD Event in 2019 and its Link With El Niño Modoki. *Geophys. Res. Lett.* 47 (7), 1–9. doi: 10.1029/2019GL086713

Doi, T., Behera, S. K., and Yamagata, T. (2020b). Wintertime Impacts of the 2019 Super IOD on East Asia. *Geophys. Res. Lett.* 47 (18), 1–9. doi: 10.1029/2020GL089456

Durack, P. J., and Wijffels, S. E. (2010). Fifty-Year Trends in Global Ocean Salinities and Their Relationship to Broad-Scale Warming. *J. Climate* 23 (16), 4342–4362. doi: 10.1175/2010JCLI3377.1

Gruber, N., Sarmiento, J. L., and Stocker, T. F. (1996). An Improved Method for Detecting Anthropogenic CO 2 in the Oceans. *Global Biogeochem. Cycle.* 10 (4), 809–837. doi: 10.1029/96GB01608

Hersbach, H., Bell, B., Berrisford, P., Biavati, G., Horányi, A., Muñoz Sabater, J., et al. (2019). "ERA5 monthly averaged data on single levels from 1979 to present," in *Copernicus Climate Change Service (C3S) Climate Data Store (CDS)*. doi: 10.24381/cds.f17050d7

Hood, E. M., Sabine, C. L., and Sloyan, B. M. (2010). "The GO-SHIP Repeat Hydrography Manual: A Collection of Expert Reports and Guidelines," in *IOCCP Report Number 14, ICPO Publication Series Number 134*. Available at: http://www.go-ship.org/HydroMan.html.

Hosoda, S., Ohira, T., and Nakamura, T. (2008). A Monthly Mean Dataset of Global Oceanic Temperature and Salinity Derived From Argo Float Observations. *JAMSTEC Rep. Res. Dev.* 8 (November), 47–59. doi: 10.5918/jamstecr.8.47

Hu, S., and Sprintall, J. (2016). Interannual Variability of the Indonesian Throughflow: The Salinity Effect. *J. Geophys. Res.: Ocean.* 121 (4), 2596–2615. doi: 10.1002/2015JC011495

Hu, S., Zhang, Y., Feng, M., Du, Y., Sprintall, J., Wang, F., et al. (2019). Interannual to Decadal Variability of Upper-Ocean Salinity in the Southern Indian Ocean and the Role of the Indonesian Throughflow. *J. Climate* 32 (19), 6403–6421. doi: 10.1175/JCLI-D-19-0056.1

Johnson, G. C., Robbins, P. E., and Hufford, G. E. (2001). Systematic Adjustments of Hydrographic Sections for Internal Consistency. *J. Atmosph. Ocean. Technol.* 18 (7), 1234–1244. doi: 10.1175/1520-0426(2001)018<1234:SAOHSF>2.0.CO;2

Kido, S., and Tozuka, T. (2017). Salinity Variability Associated With the Positive Indian Ocean Dipole and its Impact on the Upper Ocean Temperature. *J. Climate* 30 (19), 7885–7907. doi: 10.1175/JCLI-D-17-0133.1

Kido, S., Tozuka, T., and Han, W. (2019). Anatomy of Salinity Anomalies Associated With the Positive Indian Ocean Dipole. *J. Geophys. Res.: Ocean.* 124 (11), 8116–8139. doi: 10.1029/2019JC015163

Kobayashi, T., Mizuno, K., and Suga, T. (2012). Long-Term Variations of Surface and Intermediate Waters in the Southern Indian Ocean Along 32°S. *J. Oceanogr.* 68 (2), 243–265. doi: 10.1007/s10872-011-0093-5

Kouketsu, S., Doi, T., Kawano, T., Masuda, S., Sugiura, N., Sasaki, Y., et al. (2011). Deep Ocean Heat Content Changes Estimated From Observation and Reanalysis Product and Their Influence on Sea Level Change. *J. Geophys. Res.: Ocean.* 116 (3), 1–16. doi: 10.1029/2010JC006464

Kouketsu, S., and Murata, A. M. (2014). Detecting Decadal Scale Increases in Anthropogenic CO 2 in the Ocean. *Geophys. Res. Lett.* 41 (13), 4594–4600. doi: 10.1002/2014GL060516

Kouketsu, S., Murata, A., and Doi, T. (2013). Decadal Changes in Dissolved Inorganic Carbon in the Pacific Ocean. *Global Biogeochem. Cycle.* 27 (1), 65–76. doi: 10.1029/2012GB004413

Kouketsu, S., Osafune, S., Kumamoto, Y., and Uchida, H. (2017). Eastward Salinity Anomaly Propagation in the Intermediate Layer of the North Pacific. *J. Geophys. Res.: Ocean.* 122 (2), 1590–1607. doi: 10.1002/2016JC012118

Lauvset, S., Lange, N., Tanhua, T., Bittig, H., Olsen, A., Kozyr, A., et al. (2022). An updated version of the global interior ocean biogeochemical data product, GLODAPv2. 2021. *Earth Syst. Sci. Data.* 13, 5565–5589. doi: 10.5194/essd-13-5565-2021

Li, Y., and Wang, F. (2015). Thermocline Spiciness Variations in the Tropical Indian Ocean Observed During 2003-2014. *Deep-Sea. Res. Part I.: Oceanogr. Res. Pap.* 97, 52–66. doi: 10.1016/j.dsr.2014.12.004

McDougall, T. J., and Klocker, A. (2010). An Approximate Geostrophic Streamfunction for Use in Density Surfaces. *Ocean. Model.* 32 (3–4), 105–117. doi: 10.1016/j.ocemod.2009.10.006

Murata, A., Kumamoto, Y., Watanabe, S., and Fukasawa, M. (2007). Decadal Increases of Anthropogenic CO2 in the South Pacific Subtropical Ocean Along 32°S. *J. Geophys. Res.: Ocean.* 112 (5), 1–11. doi: 10.1029/2005JC003405

Nagura, M., and Kouketsu, S. (2018). Spiciness Anomalies in the Upper South Indian Ocean. *J. Phys. Oceanogr.* 48 (9), 2081–2101. doi: 10.1175/JPO-D-18-0050.1

Rao, R. R., and Sivakumar, R. (2003). Seasonal Variability of Sea Surface Salinity and Salt Budget of the Mixed Layer of the North Indian Ocean. *J. Geophys. Res.: Ocean.* 108 (C1), 3009. doi: 10.1029/2001jc000907

Reynolds, R. W., Rayner, N. A., Smith, T. M., Stokes, D. C., and Wang, W. (2002). An Improved *in Situ* and Satellite SST Analysis for Climate. *J. Climate* 15 (13), 1609–1625. doi: 10.1175/1520-0442(2002)015<1609:AIISAS>2.0.CO;2

Sabine, C. L., Feely, R. A., Key, R. M., Bullister, J. L., Millero, F. J., Lee, K., et al. (2002a). Distribution of Anthropogenic CO 2 in the Pacific Ocean. *Global Biogeochem. Cycle.* 16 (4), 30-1-30–17. doi: 10.1029/2001GB001639

Sabine, C. L., Key, R. M., Feely, R. A., and Greeley, D. (2002b). Inorganic Carbon in the Indian Ocean: Distribution and Dissolution Processes. *Global Biogeochem. Cycle.* 16 (4), 15-1-15–18. doi: 10.1029/2002GB001869

Saji, N. H., Goswami, B. N., Vinayachandran, P. N., and Yamagata, T. (1999). A Dipole Mode in the Tropical Indian Ocean. *Nature* 401 (6751), 360–363. doi: 10.1038/43854

Shi, W., and Wang, M. (2021). A Biological Indian Ocean Dipole Event in 2019. *Sci. Rep.* 11 (1), 1–8. doi: 10.1038/s41598-021-81410-5

Strutton, P. G., Coles, V. J., Hood, R. R., Matear, R. J., McPhaden, M. J., and Phillips, H. E. (2015). Biogeochemical Variability in the Central Equatorial Indian Ocean During the Monsoon Transition. *Biogeosciences* 12 (8), 2367–2382. doi: 10.5194/bg-12-2367-2015

Swift, J., and Becker, S. (2019a) *Data From Cruise 316N145_7, Exchange Version*. Available at: https://cchdo.ucsd.edu/cruise/316N145_7 (Accessed 2021-06-01).

Swift, J., and Becker, S. (2019b) *Data From Cruise 3175MB95_07, Exchange Version*. Available at: https://cchdo.ucsd.edu/cruise/3175MB95_07 (Accessed 2021-06-01).

Takaya, Y., Ishikawa, I., Kobayashi, C., Endo, H., and Ose, T. (2020). Enhanced Meiyu-Baiu Rainfall in Early Summer 2020: Aftermath of the 2019 Super IOD Event. *Geophys. Res. Lett.* 47 (22), 1–9. doi: 10.1029/2020GL090671

Thompson, B., Gnanaseelan, C., and Salvekar, P. S. (2006). Variability in the Indian Ocean Circulation and Salinity and its Impact on SST Anomalies During Dipole Events. *J. Mar. Res.* 64 (6), 853–880. doi: 10.1357/002224006779698350

Uchida, H., Murata, A., Katsumata, K., Arulannanthan, K., and Doi, T. (2021). *WHP I08N REVISIT/I07S IN 2019/2020* (Yokosuka, Japan: JAMSTEC). doi: 10.17596/0002162

Uchida, H., Nakano, T., Tamba, J., Widiatmo, J. V., Yamazawa, K., Ozawa, S., et al. (2015). Deep Ocean Temperature Measurement With an Uncertainty of 0.7 mK. *J. Atmosph. Ocean. Technol.* 32, 2199–2210. doi: 10.1175/JTECH-D-15-0013.1

Valsala, V., Sreeush, M. G., and Chakraborty, K. (2020). The IOD Impacts on the Indian Ocean Carbon Cycle. *J. Geophys. Res.: Ocean.* 125 (11), 1–18. doi: 10.1029/2020JC016485

Zhang, Y., Du, Y., Zheng, S., Yang, Y., and Cheng, X. (2013). Impact of Indian Ocean Dipole on the salinity budget in the equatorial Indian Ocean. *J. Geophys. Res. Oceans* 118, 4911–4923. doi: 10.1002/jgrc.20392

Zhang, N., Feng, M., Du, Y., Lan, J., and Wijffels, S. E. (2016). Seasonal and Interannual Variations of Mixed Layer Salinity in the Southeast Tropical Indian Ocean. *J. Geophys. Res.: Ocean.* 121 (7), 4716–4731. doi: 10.1002/2016JC011854

Conflict of Interest: The authors declare that the research was conducted in the absence of any commercial or financial relationships that could be construed as a potential conflict of interest.

Publisher's Note: All claims expressed in this article are solely those of the authors and do not necessarily represent those of their affiliated organizations, or those of the publisher, the editors and the reviewers. Any product that may be evaluated in this article, or claim that may be made by its manufacturer, is not guaranteed or endorsed by the publisher.

APPENDIX

Estimation of anthropogenic carbon changes

We estimated the changes in anthropogenic CO_2 following the methodology of Murata et al. (2007) by applying the ΔC^* method (Gruber et al., 1996) to two data collection periods (the previous cruises in 1995 and our cruise in 2019). The calculations were simplified by making the following assumptions. We defined the anthropogenic CO_2 concentration in the ocean interior (C_{anth} μmol kg^{-1}) as follows (e.g., Sabine et al., 2002a; Sabine et al., 2002b):

$$C_{anth} = C - \gamma_{c:o} \times AOU - \left\{0.5 \times (Alk - Alk_0) + C_0 + \Delta C_{diseq}\right\} \quad (1)$$

where is the Redfield ratio for carbon and DO and is 0.69 (Anderson and Sarmiento, 1994). The apparent oxygen utilization (AOU) was the difference between the observed concentration of dissolved oxygen (DO, μmol kg^{-1}) and the saturated DO concentration at each potential temperature and salinity. C (μmol kg^{-1}) and Alk (μmol kg^{-1}) are the DIC and alkalinity, respectively. Alk_0 (μmol kg^{-1}) is the preformed Alk, which is assumed to have been constant from preindustrial times to the present. C_0 (μmol kg^{-1}) is the theoretical DIC of water in equilibrium with the atmosphere without anthropogenic CO_2. ΔC_{diseq} (μmol kg^{-1}) is the difference between C in the mixed layer in equilibrium with atmospheric CO_2 and C at the time of water mass formation.

When the changes in anthropogenic CO_2 between the two data collection periods were calculated, both C_0 and A_0 were cancelled out. Furthermore, we assumed that on a decadal timescale, changes in Alk and ΔC_{diseq} were negligible, and that these values could be disregarded. We calculated the change in anthropogenic CO_2 (ΔC_{anth}, μmol kg^{-1}) over the decade as follows:

$$\Delta C_{anth} = C_{anth}(t_{2019}) - C_{anth}(t_{1995}) \quad (2)$$

where C_{anth} (t_{2019}) and C_{anth} (t_{1995}) are the normalized C values for the two sets of observations in 1995 (t_{1995}) and 2019 (t_{2019}), respectively. The values were normalized to a salinity of 35 to remove the influence of changes caused by the addition or removal of freshwater; normalization did not significantly affect the results.